ROYAL SOCIETY
OF CHEMISTRY

PAPER

Check for updates

Atomically dispersed Co²⁺ on MgAlOₓ boosting C₄₋₁₀ alcohols selectivity of ethanol valorization†

Wen-Lu Lv, Lei He, Wen-Cui Li, [iD] Bai-Chuan Zhou, Shao-Pei Lv and An-Hui Lu [iD] *

Catalytic upgrading of biomass-derived ethanol to C$_{4+}$ compounds through C−C coupling is an essential green and sustainable approach towards value-added fine chemicals. Developing catalysts to improve the selectivity of C$_{4+}$ compounds is highly desired due to the complex transformation of ethanol affording diverse species. Here, we report atomically dispersed Co^{2+} on MgAlO$_x$ as catalysts derived from layered double hydroxide (LDH) precursors for the dehydrogenation coupling of ethanol to C$_{4-10}$ alcohols. The selectivity for C$_{4-10}$ alcohols reaches 95.4% with 32.9% ethanol conversion over the optimal catalyst, Co$_{0.15}$Mg$_{2.85}$AlO$_x$, at 523 K and 0.1 MPa. A yield of 31.4% is greatly higher than that (~15%) over most of the state-of-the-art catalysts. Characterization techniques including XRD, XPS, UV-Vis and CO-IR reveal that the atomically dispersed Co^{2+} in the lattice of MgAlO$_x$ is originated from the replacement of Mg in the LDH precursor and remain stable during the reactions. Both increments of basic and acid sites are observed after Co^{2+} replacement according to the TPD-MS measurements of CO$_2$ and NH$_3$. The introduction of an appropriate amount of Co^{2+} effectively facilitates the dehydrogenation step, thus, high activity under milder conditions. Meanwhile, abundant basic and acid sites boost the following aldol condensation step resulting in ultra-high C$_{4-10}$ selectivity. These findings can shed light on sustainable heterogeneous catalytic processes.

Introduction

Catalytic conversion of biomass-derived ethanol to value-added higher aliphatic alcohols under relatively mild conditions is a green and sustainable process with a small ecological footprint.[1–3] C$_{4-10}$ alcohols are essential chemical feedstocks for various chemical processes and are widely used as solvents, extractants, and chemical intermediates.[4–6] In particular, they are desirable as biofuels or additives due to their higher energy density (29–35 MJ L^{-1}), air-to-fuel ratio, octane numbers and lower water solubility compared with ethanol.[7,8] Traditionally, three methods including the oxo process,[9,10] acetaldehyde method, or fermentation[11,12] can be used to produce C$_{4-10}$ alcohols, among which the oxo process is the most commonly used in the petrochemical industry. The oxo process involves the hydroformylation of propylene with syngas on catalysts at high pressures to produce aldehyde and hydrogenation of the aldehyde to provide *n*-butanol. The whole process is a homogeneous reaction and requires several steps to obtain the target products.

Recently, motivated by the carbon neutrality policy, the more desirable route for the production of C$_{4-10}$ aliphatic alcohols from ethanol using a one-pot process would be a renewable and low carbon footprint strategy.[13–15] Catalytic transformation of ethanol into C$_{4-10}$ alcohols has been proposed to proceed by either a direct condensation[16,17] or a Guerbet reaction.[18,19] In the former mechanism, the C−H bond in the β-position of an ethanol molecule is activated and then reacted with the −OH group of another ethanol molecule *via* dehydration reaction to form *n*-butanol. The latter mechanism involves the following three steps: dehydrogenation of ethanol to acetaldehyde, aldol condensation of the two molecules of acetaldehyde, and hydrogenation of the unsaturated aldehyde (crotonaldehyde) to generate higher alcohols. Several heterogeneous catalysts with Lewis acid and base sites, such as M-CeO$_2$/carbon,[20–22] Pd@UiO-66,[23] hydroxyapatite (HAP),[15,24–27] and mixed metal oxides[28–30] have been reported for ethanol upgrading. Among these catalysts, Mg–Al mixed oxides were particularly noteworthy mainly owing to their controllable acid/base properties, easy synthesis, and relatively high selectivity for *n*-butanol.[31] In this catalytic system, high temperature (>623 K)[32] is often necessary to achieve an acceptable yield because of the relatively weak dehydrogenation ability of Lewis acid/base sites over Mg–Al mixed oxides.[33] However, the presence of acid sites increases the dehydration of ethanol particularly at high reaction temperatures, conse-

State Key Laboratory of Fine Chemicals, Liaoning Key Laboratory for Catalytic Conversion of Carbon Resources, School of Chemical Engineering, Dalian University of Technology, Dalian 116024, P. R. China. E-mail: anhuilu@dlut.edu.cn

quently decreasing the efficiency for C–C coupling reactions.[31] Doping transition metals can promote ethanol dehydrogenation over Mg–Al mixed oxides and consequently improve the valorization process at relatively milder temperatures.[34,35] But the overall yield of C_{4-10} alcohols remains unsatisfactory (~15%) due to the large amount of dehydrogenation byproducts. A tradeoff of the dehydrogenation and C–C coupling active sites is necessary to achieve both high activity and selectivity.

In this study, we prepared the $Co_nMg_{3-n}AlO_x$ catalysts derived from CoMgAl layered double hydroxides (LDHs), which can efficiently catalyze the conversion of ethanol to C_{4-10} alcohols showing high activity and selectivity by regulating the synergetic acceleration of dehydrogenation and C–C coupling reactions. The geometric and electronic structures of the $Co_nMg_{3-n}AlO_x$ catalysts were investigated in detail using various characterization methods. Moreover, the reaction pathway was validated based on kinetic measurements.

Experimental

Catalyst preparation

CoMgAl-LDH and MgAl-LDH as the precursors for the $Co_nMg_{3-n}AlO_x$ and Mg_3AlO_x catalysts were synthesized using a coprecipitation method according to the literature.[36,37] Taking the $Co_{0.15}Mg_{2.85}AlO_x$ catalyst as an example, a mixed solution (0.6 mol L^{-1}) containing $Mg(NO_3)_2 \cdot 6H_2O$, $Al(NO_3)_3 \cdot 9H_2O$, and $Co(NO_3)_2 \cdot 6H_2O$ with a molar ratio of 0.15 : 2.85 : 1 was prepared and added dropwise to the mixed $Na_2CO_3/NaOH$ solution. Then, the pH was adjusted to 10 using a 3 mol L^{-1} NaOH aqueous solution. Under steady titration and vigorous mixing, a precipitate slurry was formed that was then aged for 18 h at 338 K. The precipitate was separated by filtration, washed with deionized water repeatedly, and then dried at 323 K overnight. Finally, the dry precursor was calcined at 873 K in the air for 2 h with a temperature ramp of 5 K min^{-1}. A series of catalysts were prepared by varying the Co molar ratio from 0 to 0.6. The actual Co content of the catalysts was determined using an Optima 2000DV instrument by ICP-OES.

The reference $Co_{0.15}Mg_{2.85}AlO_x$-IM catalyst was prepared using a wet-impregnation method. Briefly, $Mg_{2.85}AlO_x$ was impregnated with an aqueous solution of $Co(NO_3)_2 \cdot 6H_2O$ containing the same Co content as the $Co_{0.15}Mg_{2.85}AlO_x$ catalyst and held at room temperature for 2 h. The precursor was dried at 323 K in flowing air and calcined at 823 K for further 2 h in static air to obtain the reference catalyst.

Characterization

Powder X-ray diffraction (XRD) patterns were obtained with a PANalytical X'pert Pro Super X-ray diffractometer using Cu Kα radiation (40 kV, 40 mA, λ = 0.15418 nm) at a scanning speed of 5° min^{-1} over the range of 10–90°. X-ray photoelectron spectroscopy (XPS) was performed with a PHI Versaprobe 5000 spectrometer equipped with an Al Kα X-ray source. Before the experiments, the samples were reduced with hydrogen at

773 K for 2 h and sealed in a vessel with the protection of Ar to avoid oxidation of the samples during the transfer.

The aberration-corrected high-angle annual dark-field scanning transmission electron microscopy (AC-HAADF-STEM) analysis was performed on an FEI Themis Z microscope equipped with a spherical aberration corrector and operated at 300 kV. The high-resolution elemental mapping of energy dispersive X-ray (EDX-mapping) spectroscopy images were obtained using a Titan ETTEM Themis and Super X EDS equipped on the microscope.

The UV-Vis DR spectra of powder samples were recorded on a UV-vis spectrophotometer (Cary-5000) with a diffuse reflectance attachment of an integration sphere. The scanning was performed in the wavelength range of 200–800 nm at room temperature for a sample loaded in a transparent quartz cell. The reflectance of $BaSO_4$ was used as a reference for the baseline of various samples. CO-FTIR experiments were carried out in a custom batch reactor. Spectra were recorded after exposure to 10^{-5} Torr CO at 123 K on a Bruker 70 V spectrometer. An *in situ* IR test was performed on a Thermo Scientific Nicolet 6700 spectrometer equipped with an MCT detector.

Temperature-programmed reduction under H_2 atmosphere (H_2-TPR) was carried out on a Micromeritics AutoChem II 2920 system. Catalysts (40–60 meshes) were loaded into quartz U tubes and then heated in 8 vol% H_2/Ar at a heating rate of 10 K min^{-1} up to 873 K. A thermal conductivity detector (TCD) was used to calculate the amount of hydrogen consumption during the experiment. The type and number of basic and acidic sites on various catalyst surfaces were determined by temperature programmed desorption mass spectrometry (TPD-MS) of CO_2 and NH_3, respectively, using a Micromeritics AutoChem II 2920 system as well.

Catalytic activity measurements

All experiments were performed in a quartz-tube, packed-bed reactor (8 mm i.d.) under atmospheric pressure. Before the reaction, a 200 mg catalyst was pretreated at 723 K for 2 h using 8 vol% H_2 in N_2. Ethanol (weight hourly space velocity, WHSV = 0.96 h^{-1}) was introduced into the evaporator using a syringe pump and carried into the reactor by N_2. A gas chromatograph with a flame ionization detector (GC-FID) was connected to the reactor outlet to quantify the products. Their identities were confirmed by GC-MS analysis (Agilent 7890A GC, interfaced with 5975C MS). The carbon balance for all the samples was better than 98%. The conversion and selectivity were calculated by calibration area normalization. Details of the calculations for ethanol conversion and product selectivity are shown in the ESI.†

Results and discussion

Catalytic performance in ethanol upgrading

The Co molar ratio had a critical influence on the catalytic performances, and its effects on C_{4-10} alcohol selectivity and ethanol conversion were therefore investigated. As shown in
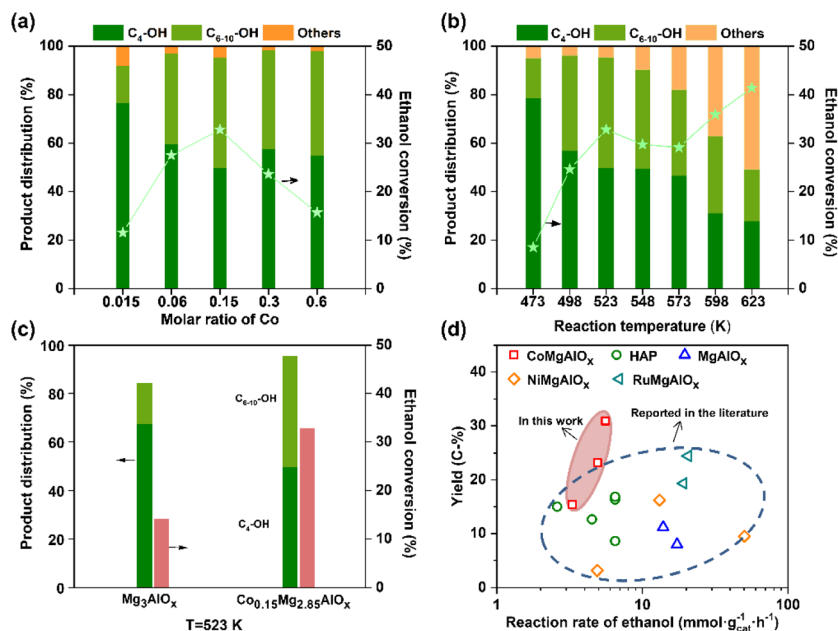
Fig. 1 Catalytic performance. (a) Ethanol conversions over $Co_nMg_{3-n}AlO_x$ catalysts with various Co molar ratios. Reaction activity was measured at 523 K in a feed gas of 5.6 vol% C_2H_5OH/N_2 with a WHSV of 0.96 $g_{C_2H_5OH} \, g_{cat}^{-1} \, h^{-1}$. (b) Ethanol conversions over the $Co_{0.15}Mg_{2.85}AlO_x$ catalyst at various temperatures. Reaction activity was measured over $Co_{0.15}Mg_{2.85}AlO_x$ at 498–623 K in a feed gas of 5.6 vol% C_2H_5OH/N_2 with a WHSV of 0.96 $g_{C_2H_5OH} \, g_{cat}^{-1} \, h^{-1}$. (c) Comparison of ethanol conversion and product distribution over $Co_{0.15}Mg_{2.85}AlO_x$ and Mg_3AlO_x at 523 K in a feed gas of 5.6 vol% C_2H_5OH/N_2 with a WHSV of 0.96 $g_{C_2H_5OH} \, g_{cat}^{-1} \, h^{-1}$. (d) Yields of C_{4-10} alcohols *versus* the ethanol reaction rate for catalysts described in this work and in the literature (Table S1†).

Fig. 1a, for catalysts with 0.015 to 0.15 cobalt molar ratio, ethanol conversion increased from 11.5% to 32.9%. Nevertheless, further increasing the Co molar ratio to 0.6 apparently decreased the ethanol conversion. Over the optimal $Co_{0.15}Mg_{2.85}AlO_x$ catalyst, the selectivity for total C_{4-10} aliphatic alcohols reached 95.4%, which is greatly higher than that of the catalysts reported in previous articles (Table S1†).

The product distribution in ethanol conversion is sensitive to the reaction temperature, thus the effects of temperature on ethanol conversion and C_{4-10} alcohol selectivity were investigated. As shown in Fig. 1b, increasing the temperature from 473 to 523 K caused a linear increase in ethanol conversion from 8.5% to 32.9%, and the selectivity for the C_{4-10} alcohols remained above 90% over the $Co_{0.15}Mg_{2.85}AlO_x$ catalyst. Further increasing the temperature to 623 K increased the ethanol conversion to 41.4%, but the overall selectivity for the C_{4-10} alcohols decreased to 49.2% due to the large generation of dehydration/dehydrogenation byproducts, including ethylene, ethylether, acetaldehyde, *etc.* The ethanol conversion slightly decreased when the temperature increased from 523 to 573 K due to the partial coverage of active sites by condensed byproducts according to the carbon balance (Table S3†). The following recovery of ethanol conversion corroborates that the inhibition due to condensed product deposition was decomposed at high temperatures.[6] Considering the reaction efficiency and selectivity, the reaction temperature was maintained below 573 K in the following study. The catalytic performance of $Co_{0.15}Mg_{2.85}AlO_x$ was compared with that of the

Mg_3AlO_x catalyst at 573 K (Fig. 1c). We observe that the increment of Co in $MgAlO_x$ is associated with a large increase in catalyst productivity, and the ethanol conversion using $Co_{0.15}Mg_{2.85}AlO_x$ (32.9%) is more than one time as that using Mg_3AlO_x (14.0%). In addition, the selectivity for C_{4-10} alcohols also increased from 83.3% to 95.4%.

Combined with the catalytic performance over these two catalysts at 493 K, 548 K, and 573 K (Fig. S1†), as the temperature increases, byproducts can be detected over all catalysts, which further indicates that the addition of Co significantly increases the alcohol condensation yield by raising ethanol conversion at lower temperatures. To shed light on the features of $Co_{0.15}Mg_{2.85}AlO_x$, the yields of higher alcohols in the literature are shown in Fig. 1d as a function of the reaction rate. The yield (31.4%) of C_{4-10} alcohols is greatly higher than that of (*ca.* 15%) using the best state-of-the-art catalyst, showing that $Co_{0.15}Mg_{2.85}AlO_x$ is competent for the efficient production of C_{4-10} alcohols from ethanol.

As the Co species were introduced during the deposition step of the catalyst preparation process, the replacement of Co^{2+} for Mg^{2+} in Mg_3AlO_x can result in highly dispersed Co sites over the $Co_{0.15}Mg_{2.85}AlO_x$ catalyst. To reveal the influence of Co agglomeration states on the catalytic performance, $Co_{0.15}Mg_{2.85}AlO_x$-IM was synthesized with fewer replaced Co species over the catalyst through the incipient method with the same Co loading. As shown in Fig. S2,† the predominant product was *n*-butanol, with a selectivity of 68.8% and only 12.9% ethanol conversion. The order of the ethanol conversion

over the three catalysts was $Co_{0.15}Mg_{2.85}AlO_x > Mg_3AlO_x > Co_{0.15}Mg_{2.85}AlO_x$-IM. The order of the C_{4-10} alcohol selectivity over the three catalysts was $Co_{0.15}Mg_{2.85}AlO_x > Co_{0.15}Mg_{2.85}AlO_x$-IM $> Mg_3AlO_x$. To make a better comparison of the role of different status of the Co species, the $Co_{0.15}Mg_{2.85}AlO_x$ catalyst was reduced at 973 K to obtain more metallic Co for the ethanol conversion test. The selectivity of C_{4-10} alcohols still remained consistently around 95%, while the conversion of ethanol decreased by ~7% (Fig. S3†). It indicates that metallic Co can also facilitate this reaction, but with a relatively lower activity. These results demonstrate that the amount and status of the Co species are the key factors influencing ethanol valorization, which were further investigated as follows.

Characterization of the Co species and the acid-basic properties

Prior to the characterization, the $Co_{0.15}Mg_{2.85}AlO_x$ catalyst was pretreated at 673 K in 8 vol% H_2/N_2. As shown in Fig. 2 and Fig. S4,† polycrystalline mixed oxides can be observed with homogeneously distributed elements. The crystal lattice distance of 0.209 nm can be attributed to the (002) plane of the typical phase of the mixed oxide derived from MgAl-LDH. From the selected area electron diffraction (SAED) image, the observation of the diffraction rings was coordinated with the HRTEM results. The AC-HAADF-STEM images and the corresponding maps of Co, Mg, Al, and O for the $Co_{0.15}Mg_{2.85}AlO_x$ catalyst further indicate that the Co species were atomically dispersed within the mixed oxide matrix without aggregation. Additionally, the TEM images of the used $Co_{0.15}Mg_{2.85}AlO_x$ catalyst in Fig. S5† show an unchanged structure compared with the fresh catalyst, indicating the excellent stability of the catalyst.

The XRD measurements were carried out to analyze the phase structure of the catalysts. Fig. 3a shows the XRD patterns of $Co_nMg_{3-n}AlO_x$ obtained after calcination of CoMgAl-LDHs at 823 K. All the patterns resemble a periclase highly dispersed metal mixed oxide phase. The major diffraction peaks at 43.2° and 62.6° can be indexed to the (200) and (220) planes of typical Mg–Al mixed oxide.[38] Moreover, there are no peaks assigned to crystalline metallic cobalt or cobalt oxides detected over $Co_{0.15}Mg_{2.85}AlO_x$, indicating the high dispersity of the cobalt species,[39] which is coordinated with the TEM observation. Meanwhile, the structure of the spent $Co_{0.15}Mg_{2.85}AlO_x$ catalyst remains the same, indicating the excellent stability of this catalyst (Fig. S6†). Besides, the XRD patterns of the impregnated sample $Co_{0.15}Mg_{2.85}AlO_x$-IM are similar to those of $Co_{0.15}Mg_{2.85}AlO_x$ (Fig. S7†). Only separated Co_3O_4 phase can be observed when the Co molar ratio increased to 0.6, indicating the highly dispersible ability of Co for the LDH-derived catalysts.

Hydrogen temperature-programmed reduction (H_2-TPR) characterization was used to study the type of metal species during the reaction. As shown in Fig. 3b, there are no obvious reduction peaks observed below 873 K on the catalysts with a Co molar ratio lower than 0.3. It indicates that Co in the $Co_{0.15}Mg_{2.85}AlO_x$ catalyst is difficult to reduce at the pretreatment reduction temperature (673 K). Two H_2 consumption peaks appeared at *ca.* 493 K and 673 K for the $Co_{0.6}Mg_{2.4}AlO_x$ catalyst, which can be attributed to the reduction of $Co_3O_4 \rightarrow CoO$. This result corresponds to the results of the XRD analysis.

The influence of cobalt contents on the structural properties of the produced mixed oxides was also studied by nitrogen adsorption–desorption. The nitrogen adsorption–desorption isotherms and pore size distributions are shown in Fig. 3c and d for the Mg_3AlO_x, $Co_{0.15}Mg_{2.85}AlO_x$, and $Co_{0.15}Mg_{2.85}AlO_x$-IM catalysts. The average pore size, total pore volume and surface area are calculated and listed in Table S2.† All of the three catalysts show reversible type IV isotherms with the hysteresis loop falling, which are characteristic of mesoporous materials. As shown in Fig. 3d, Mg_3AlO_x without cobalt has a wide pore distribution with maxima at 2.6 and 20.0 nm, corresponding to small mesopores and large mesopores. $Co_{0.15}Mg_{2.85}AlO_x$ has a narrow pore size distribution with a sharp maximum at 9.9 nm. The $Co_{0.15}Mg_{2.85}AlO_x$-IM has the widest pore size distri-
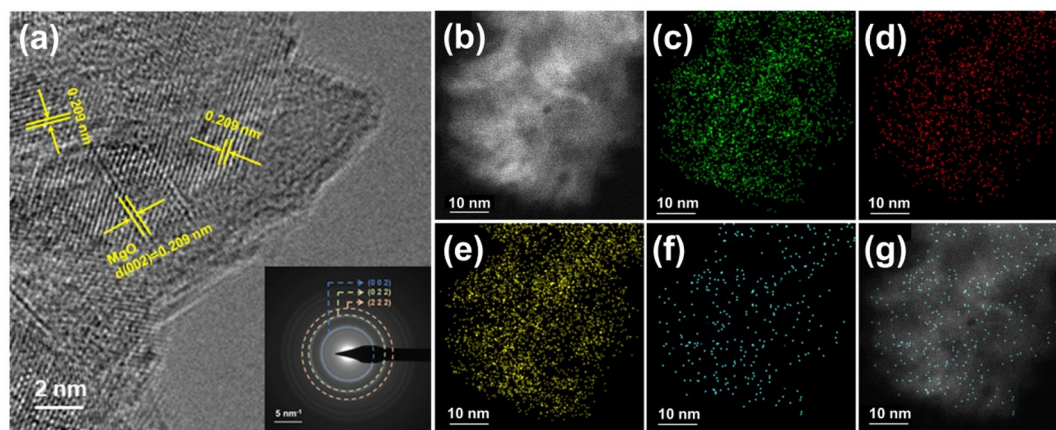

Fig. 2 (a) HRTEM with fast Fourier transform (FFT) of the electron diffraction data. (b) AC-HAADF-STEM image and EDS elemental-mapping analysis of (c) Mg, (d) Al, (e) O, and (f) Co and (g) the overlayer of Co distribution and the HAADF image for the $Co_{0.15}Mg_{2.85}AlO_x$ catalyst.

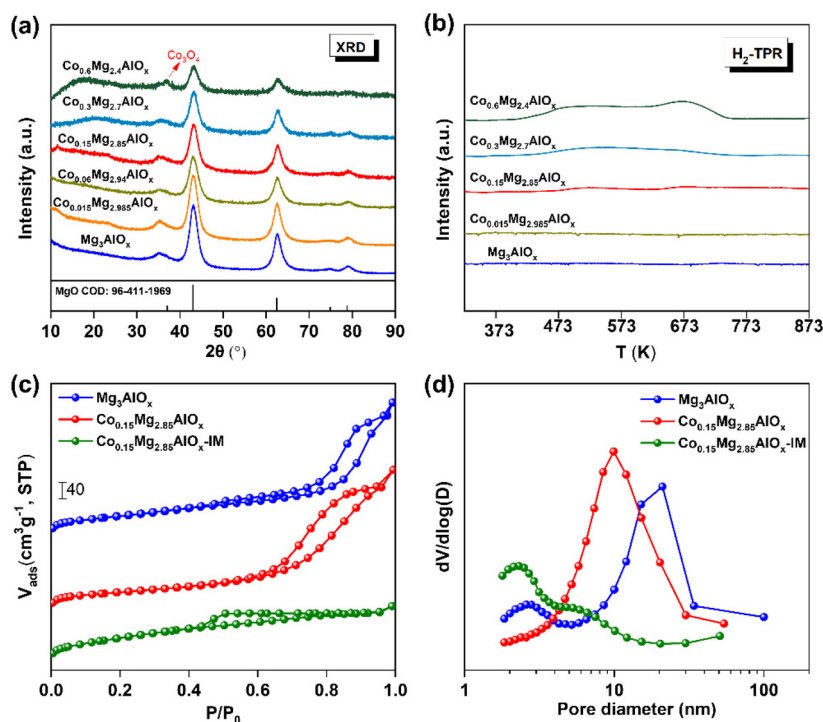**Fig. 3** (a) XRD profiles of the $Co_nMg_{3-n}AlO_x$ catalysts, (b) H_2-TPR profiles for the $Co_nMg_{3-n}AlO_x$ catalysts, (c) nitrogen sorption isotherms and (d) pore size distributions of the Mg_3AlO_x, $Co_{0.15}Mg_{2.85}AlO_x$ and $Co_{0.15}Mg_{2.85}AlO_x$-IM catalysts.

bution among the three samples. The total pore volumes and pore sizes of Mg_3AlO_x and $Co_{0.15}Mg_{2.85}AlO_x$ are similar. Although $Co_{0.15}Mg_{2.85}AlO_x$-IM has the highest surface area, it has lower pore volume and smaller pore size, which may be due to the occupation of Co_3O_4 particles over the large mesopores of Mg_3AlO_x.

XPS measurements were carried out for $Co_{0.15}Mg_{2.85}AlO_x$ and Mg_3AlO_x catalysts to gain more insight into the chemical state of the active species. The obtained survey scan of $Co_{0.15}Mg_{2.85}AlO_x$ is presented in Fig. S8.† In Fig. 4a, the peaks with binding energies (BE) of 780.9 and 796.7 eV for $Co_{0.15}Mg_{2.85}AlO_x$ represent Co $2p_{3/2}$ and Co $2p_{1/2}$ with the spin–orbit splitting of 15.6 eV ($\Delta E = E(Co\ 2p_{1/2}) − E(Co\ 2p_{3/2})$), which can be assigned to typical Co^{2+}.[40,41] The appearance of satellite peaks at 786.6 and 803.0 eV further illustrates that cobalt is present in the form of Co^{2+}. Fig. 4b shows the O $1s$ BE at 532.1, 530.8 and 529.5 eV, corresponding to the absorbed molecular water O_γ (532–533 eV), adsorbed OH groups O_β (530–531 eV), and lattice oxygen O_α (528–529 eV), respectively.[42–44] The lattice oxygen $O^{2−}$ interacts with cobalt and magnesium resulting in the formation of the Co–O–Mg/Mg–O–Mg bonds. The O $1s$ peak position and full width at half-maximum (FWHM) of $Co_{0.15}Mg_{2.85}AlO_x$ are similar to those of Mg_3AlO_x, but the intensity of the peak is slightly higher for $Co_{0.15}Mg_{2.85}AlO_x$, which can be originated from the introduction of Co^{2+} influencing the nearby O states. XPS was further utilized to analyze the surface composition of $Co_{0.60}Mg_{2.40}AlO_x$. The obtained Co $2p$ spectrum for the $Co_{0.60}Mg_{2.40}AlO_x$ catalyst exhibited two deconvoluted fitting

peaks with the BEs at about 780.1 and 780.9 eV, respectively, attributed to the Co^{3+} and Co^{2+} species (Fig. S9a†). As seen in Fig. S9b,† the intensity of the lattice oxygen $O^{2−}(O_\alpha)$ peak slightly reduced with the existence of Co^{3+}.

Being a late transition metal, cobalt with different oxidation states and coordination geometries would respond to UV-vis. As shown in Fig. 4c, the UV-vis spectrum recorded in diffuse reflectance of the fresh $Co_{0.15}Mg_{2.85}AlO_x$ catalyst exhibits three absorption peaks at 509, 597, and 678 nm, which can be assigned to the $^4A_2(F) \rightarrow {}^4T_1(P)$ transition of Co(II) ions in tetrahedral coordination.[45,46] Meanwhile, the peak at 252 nm can be referred to a low-energy charge transfer between the oxygen ligands and central Co(II) ions in a tetrahedral symmetry structure.[47,48] As shown in Fig. S10,† the UV-vis spectrum recorded in diffuse reflectance of the unreduced $Co_{0.15}Mg_{2.85}AlO_x$ catalyst exhibits an absorption peak at 656 nm, which can be assigned to the $^4T_{1g}(F) \rightarrow {}^4A_{2g}(F)$ transition of Co(II) ions in octahedral coordination.[49] The ethanol conversion over the unreduced catalyst showed a slight decrease (Fig. S11†), indicating the importance of oxidation states and coordination geometries of cobalt. Moreover, the positions of the absorption peaks are almost the same for the used $Co_{0.15}Mg_{2.85}AlO_x$ catalyst compared with the fresh sample, implying that the Co^{2+} species still remain after the reaction.

The local chemical environment of Co^{2+} was further probed by IR spectroscopy with CO as the probe. Under ambient CO pressure at 298 K, no adsorbed CO was detected on either Mg_3AlO_x or $Co_{0.15}Mg_{2.85}AlO_x$, which reconfirms the absence of

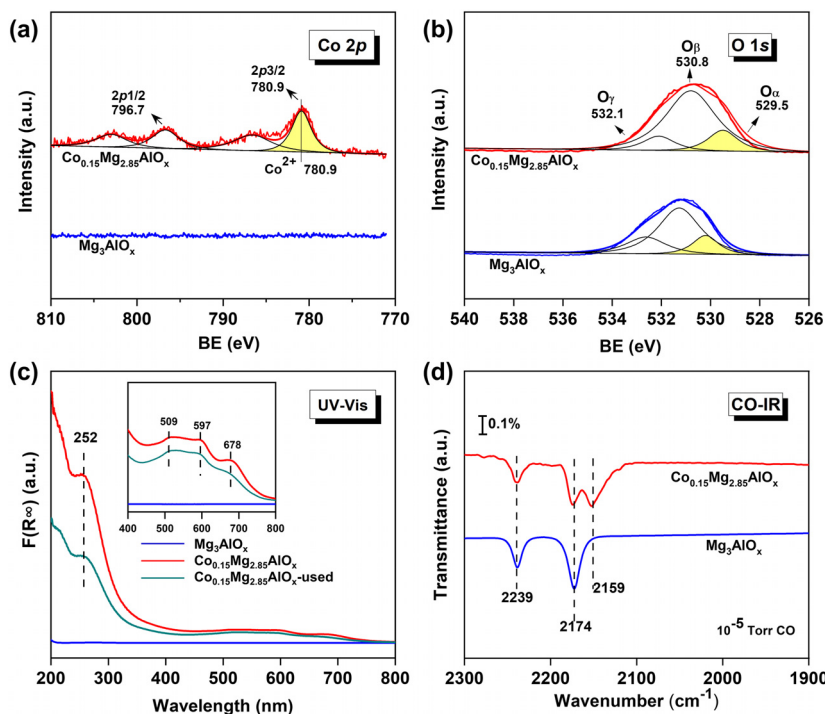**Fig. 4** Characterization of $Co_{0.15}Mg_{2.85}AlO_x$ and Mg_3AlO_x: (a and b) comparison of the Co 2p and O 1s XP spectra for the two materials. (c) UV-vis DRS profiles of Mg_3AlO_x, $Co_{0.15}Mg_{2.85}AlO_x$, and used $Co_{0.15}Mg_{2.85}AlO_x$. (d) CO-IR spectra, recorded at 123 K.

metallic Co nanoparticles even after pretreatment under H_2 at 673 K.[50] From the CO-IR analysis on Mg_3AlO_x at a low temperature (123 K) in Fig. 4d, the peaks at 2174 and 2239 cm^{-1} should be attributed to the CO–Mg^{2+} and CO–Al^{3+} species.[51,52] These two bands still exist from the spectrum of $Co_{0.15}Mg_{2.85}AlO_x$, but there is a new sharp peak observed at 2151 cm^{-1}, corresponding to CO bonded to the Co^{2+} sites.[50,53] Additionally, the absence of bands with the wavenumber above 2060 cm^{-1} and 2190 cm^{-1} indicates the absence of the CO–Co^0 species and the CO–Co^{3+} species over the $Co_{0.15}Mg_{2.85}AlO_x$ catalyst.

The acid–base pair has a critical influence on the coupling step for ethanol upgrading. Under this consideration, the acid and basic properties of the catalysts were investigated using NH_3-TPD and CO_2-TPD. As seen in Fig. S12a,† the peaks at the range of 373–573 K were observed for all catalysts, corresponding to NH_3 desorption from the acid sites. Based on the desorption peak area, the total amounts of acid sites were calculated and are listed in Table 1. It indicates that the acid sites

increase linearly along with the Co^{2+} contents. For mixed metal oxides, Lewis acid sites mainly originated from the Al^{3+} cations, and other unsaturated divalent metal cations, *e.g.* Mg^{2+}, and Co^{2+}, have also been shown to provide catalysts with some Lewis acid sites. In this case, the introduction of Co^{2+} increases the concentration of unsaturated metals on the surface, thus leading to enhanced acid sites, which is in accordance with the previous report.[39]

In Fig. S12b† the CO_2-TPD profiles show three CO_2 desorption peaks in the temperature range of 423–573 K, attributed to the superposition of CO_2 desorption from weak (OH^- groups), medium strong (Me^{n+}–O^{2-} pairs), and strong (O^{2-}) basic strengths, respectively. The amount of CO_2 desorbed in these peaks allows us to calculate the number of basic sites, as reported in Table 1. The $Co_{0.15}Mg_{2.85}AlO_x$ catalyst possesses the highest concentration of basic sites. It may be originated from the Co^{2+} cations replacing Mg in the mixed oxide. In this case, irregularities and defects are created on the oxide surface to compensate the generated positive charge, making the adja-

Table 1 Chemical properties of the Mg_3AlO_x and $Co_nMg_{3-n}AlO_x$ catalysts

Catalyst	Co content (wt%)	Basic sites ($\mu mol\ g^{-1}$)	Basic sites ($\mu mol\ g^{-1}$)			Acid sites ($\mu mol\ g^{-1}$)
			Weak	Medium	Strong	
Mg_3AlO_x	0	257.0	125.9(49%)	77.1(30%)	54.0(21%)	38.7
$Co_{0.06}Mg_{2.94}AlO_x$	1.8	291.2	107.7(37%)	113.6(39%)	69.9(24%)	56.4
$Co_{0.15}Mg_{2.85}AlO_x$	4.8	321.7	131.9(41%)	122.2(38%)	67.6(21%)	89.4
$Co_{0.60}Mg_{2.40}AlO_x$	18.5	203.9	104.0(51%)	69.3(34%)	30.6(15%)	102.8

cent oxygen anions coordinatively unsaturated, which is in line with the XPS results. With a further increase in the molar ratio of Co, *e.g.* $Co_{0.60}Mg_{2.40}AlO_x$, the concentration of the basic site decreased, in line with the XPS results. Combined with the XRD results, this observation can be explained by the formation of Co_3O_4, and the phase segregation occurs causing the density of basic sites to drop.

Combining the above characterization results, the introduction of an appropriate amount of Co^{2+} could optimize the concentration of basic and acid sites on the Mg–Al mixed oxide catalyst surface, and a better relevance is established between the concentrate change of basic sites and catalytic performance. Excessive Co addition leads to the phase separation of Co_3O_4 as that for the $Co_{0.60}Mg_{2.40}AlO_x$ catalyst, which results in the decrease of basic sites with weakened C–C coupling ability. Therefore, the atomically dispersed Co^{2+} may simultaneously promote the dehydrogenation of ethanol and the following condensation steps *via* adjusting the acid–basic properties, thus, achieving ethanol conversion to C_{4-10} alcohols with over 95% selectivity.

Mechanistic investigation

In order to gain deep insight into the excellent reactivity of the $Co_{0.15}Mg_{2.85}AlO_x$ catalyst and the function of the Co^{2+} sites, kinetic measurements were conducted for the whole reaction. The activation energies of the Mg_3AlO_x and the $Co_{0.15}Mg_{2.85}AlO_x$ catalysts were calculated and are shown in Fig. 5. The values are similar, *i.e.* 61.6 kJ mol^{-1} for Mg_3AlO_x and 59.5 kJ mol^{-1} for $Co_{0.15}Mg_{2.85}AlO_x$, suggesting that the reaction on both catalysts proceeds in a rather similar pathway. Compared with previous reports, the value of the activation energy is quite similar to the ethanol dehydrogenation (~67 kJ mol^{-1}) over Cu-based catalysts,[54] indicating that the rate-determining step may be the dehydrogenation step, which is similar to the previous literature.[28,35,55,56]

To further elucidate the function of adding Co^{2+}, the product distribution depending on ethanol conversion is obtained by varying the weight hourly space velocity (WHSV).

As shown in Fig. 5b, selectivity extrapolated to near zero conversion demonstrates that acetaldehyde (C_2H_4O) is the sole primary product on $Co_{0.15}Mg_{2.85}AlO_x$, obtained directly from ethanol dehydrogenation. At lower ethanol conversion, the *n*-butanol selectivity continuously increased with the rising of the ethanol conversion, and the amount of acetaldehyde decreased correspondingly. With the consumption of acetaldehyde, 2-butenal (C_4H_6O) forms, through self-coupling of acetaldehyde[57,58]; however, the concentration of 2-butenal is much lower than those of butanal and *n*-butanol, suggesting that the hydrogenation reaction of 2-butenal more easily takes place. Additionally, the butanal selectivity soon reaches a plateau as it is hydrogenated to *n*-butanol using hydrogen obtained from ethanol dehydrogenation as the H-donor. At higher ethanol conversion, the selectivity towards C_{6-10} alcohols and the average carbon number of alcohol products increased, which suggests that *n*-butanol participates in the reaction to form higher alcohols. The possible reaction pathway for ethanol conversion is proposed to proceed through the "Guerbet" route according to the results.

The increase of Co^{2+} leads to a significant enhancement of the ethanol conversion from 14.2 to 32.9%, and the selectivity of acetaldehyde extrapolated to near zero conversion over the Co^{2+} doped catalyst is visibly higher. The above results further confirm the vital role of ionic Co in the dehydrogenation of ethanol to acetaldehyde. As reported in the literature, the ionic Co species has been proved to be active for the dehydrogenation processes both experimentally and theoretically.[59,60] Considering the existence of hydrogen during the reaction, it is possible that the ionic Co participates in the reaction in the form of $Co^{\delta+}$ ($0 < \delta < 2$) or the mixture of Co^0/Co^{2+}. With the increase in ethanol conversion, Mg_3AlO_x gradually shows a higher selectivity to acetaldehyde. This finding validates that ionic Co favors the aldol condensation of the produced acetaldehyde. Additionally, the selectivity to C_{6-10} alcohols is still distinctly higher on $Co_{0.15}Mg_{2.85}AlO_x$ than that on Mg_3AlO_x, which indicates that the Co^{2+} content could further promote the C–C coupling reaction to form higher aliphatic alcohols.
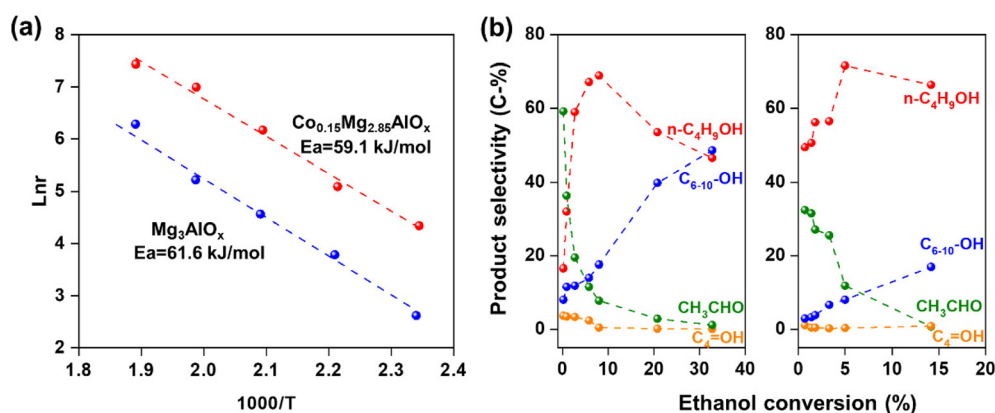

Fig. 5 (a) Arrhenius plots of the reaction rate over the reduced catalysts at 423–553 K. (b) Dependence of the product distributions as a function of the ethanol conversion over $Co_{0.15}Mg_{2.85}AlO_x$ and Mg_3AlO_x. The dashed lines are present only to guide the eye.

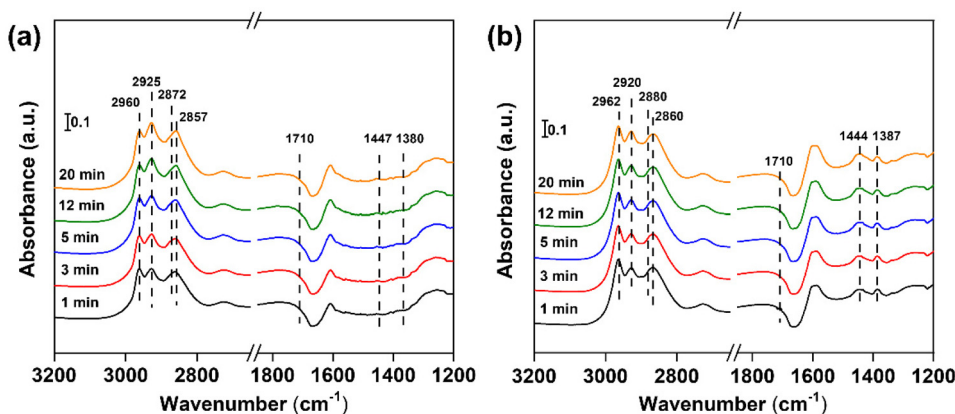**Fig. 6** *In situ* DRIFTS recorded over (a) $Co_{0.15}Mg_{2.85}AlO_x$ and (b) Mg_3AlO_x, both at 523 K after one dose of ethanol (5×10^{-8} mol) using ~40 mg of the catalyst.

The effect of residence time on the product yield on Mg_3AlO_x and $Co_{0.15}Mg_{2.85}AlO_x$ was determined in order to further probe the function of Co^{2+}. As seen in Fig. S13,† the initial product yields are plotted with ethanol conversion as a function of residence time over Mg_3AlO_x and $Co_{0.15}Mg_{2.85}AlO_x$, where the local slopes of the curves reflect the instantaneous formation rates of each product. The sigmoidal shape of the acetaldehyde yield curve and its high initial slope suggest that acetaldehyde is the primary product directly formed from ethanol dehydrogenation. It showed a volcano curve with increasing residence time due to acetaldehyde conversion to larger oxygenates in secondary condensation reactions. These results support that *n*-butanol and higher alcohols forms *via* the "Guerbet" reaction.

The sharper initial slope for the acetaldehyde yield curve represents the higher formation rate of acetaldehyde over $Co_{0.15}Mg_{2.85}AlO_x$, which illustrates the excellent ability of Co^{2+} for ethanol dehydrogenation at the first step of the reaction. The higher slope of the butanal and *n*-butanol yield curve is observed over $Co_{0.15}Mg_{2.85}AlO_x$ indicating that Co^{2+} promotes the acetaldehyde aldol condensation reactions and hydrogenation reaction. Meanwhile, the C_{6-10} alcohols yield shows a shaper increase, suggesting that Co^{2+} supported on Mg_3AlO_x remarkably promotes the C–C coupling reaction. Overall, the introduction of Co^{2+} on Mg_3AlO_x not only motivates the dehydrogenation of ethanol but also obviously favours the aldol condensation of the produced acetaldehyde and further promotes the hydrogenation and C–C coupling reaction, thus suppressing the intermolecular dehydration to other byproducts.

Next, observation of surface species on these two catalysts was conducted by *in situ* IR to investigate the role of Co^{2+} in ethanol coupling to higher carbon alcohols. Before the experiment, every sample (~40 mg) was placed in the cell and reduced at 623 K for 1 h under the 8% H_2/N_2 atmosphere. Then, the temperature was cooled down to 523 K under the flowing N_2 atmosphere to collect the background spectrum. The amount of ethanol (5×10^{-8} mol) delivered to the cell was controlled by a sample loop and the saturated vapor pressure at a given temperature. Then ethanol vapor carried by N_2 was

fed into the chamber through a bubbler for 20 min at 523 K. The corresponding DRIFT spectra were collected in the overall process. As shown in Fig. 6a, pronounced peaks are observed in the ν(C–H) region in the first 1 min. The bands around 2960, 2920, 2880 and 2860 cm^{-1} can be assigned to $\nu_{as}(CH_3)$, $\nu_{as}(CH_2)$, $\nu_s(CH_3)$ and $\nu_s(CH_2)$ of aliphatic alcohols, respectively. The intensity of peaks centered at around 2920 cm^{-1} becomes more prominent as the reaction proceeds, indicating that more –CH_2 groups were formed by the C–C coupling reaction. It was noticeable that the intensity of $\nu_{as}(CH_2)$ was more evident on $Co_{0.15}Mg_{2.85}AlO_x$, demonstrating the excellent ability of Co^{2+} for C–C coupling under the same reaction conditions. Two additional bands appeared (Fig. 6b) around 1440 and 1380 cm^{-1} that can be assigned to the scissoring vibrations of the –CH_2 and –CH_3 groups in ethoxide, indicative of the redundant unconverted ethanol species on the Mg_3AlO_x catalyst. However, fewer ethoxide bands can be found on $Co_{0.15}Mg_{2.85}AlO_x$ indicating that ethanol converted soon due to the catalytic role of Co^{2+}. Unexpectedly, no signal at ~1710 cm^{-1} typically assigned to the ν(C=O) mode of acetaldehyde is detected. That might because of the unsatisfactory time resolution. The evolution of the detected species indicated that Co^{2+} supported on the $Co_{0.15}Mg_{2.85}AlO_x$ catalyst promoted the C–C coupling reaction to higher alcohols because of the higher distribution and stability of the "–CH_2" formed.

Conclusions

In conclusion, ethanol was continuously converted to higher aliphatic alcohols over $Co_nMg_{3-n}AlO_x$ catalysts in a fixed-bed reactor under mild conditions. Over the best catalyst, the C_{4-10} alcohols selectivity over the $Co_{0.15}Mg_{2.85}AlO_x$ (4.8 wt% Co) catalyst reached 95.1% with 32.9% ethanol conversion under relatively mild conditions (523 K, 0.1 MPa), thereby showing nearly 30% yield of C_{4-10} alcohols. This yield is greatly higher than that using the state-of-the-art catalysts (15%). The reaction pathway is suggested as the "Guerbet" route, including

dehydrogenation, aldol condensation and hydrogenation. The atomically dispersed Co^{2+} facilitated ethanol dehydrogenation and thus improved the activity at relatively low temperatures. Meanwhile, the increment of the amount of basic and acid sites further promoted the following aldol condensation. The numbers of metal, acid, and basic sites were well balanced on the $Co_{0.15}Mg_{2.85}AlO_x$ catalyst, thus accelerating the "Guerbet" reaction and boosting higher alcohols production.

Conflicts of interest

There are no conflicts to declare.

Acknowledgements

References

1 A. C. Wilkie, K. J. Riedesel and J. M. Owens, *Biomass Bioenergy*, 2000, **19**, 63–102.

2 C. M. Moore, O. Staples, R. W. Jenkins, T. J. Brooks, T. A. Semelsberger and A. D. Sutton, *Green Chem.*, 2017, **19**, 169–174.

3 B. Zhou, Q. Wang, X. Weng, L. He, W. Li and A. Lu, *ChemCatChem*, 2020, **12**, 2341–2347.

4 T. L. Jordison, C. T. Lira and D. J. Miller, *Ind. Eng. Chem. Res.*, 2015, **54**, 10991–11000.

5 F. Xin, W. Zhang and M. Jiang, *Trends Biotechnol.*, 2019, **37**, 923–926.

6 M. F. Guo, M. J. Gray, H. Job, C. Alvarez-Vasco, S. Subramaniam, X. Zhang, L. Kovarik, V. Murugesan, S. Phillips and K. K. Ramasamy, *Green Chem.*, 2021, **23**, 8030–8039.

7 N. M. Eagan, M. Kumbhalkar, J. S. Buchanan, J. A. Dumesic and G. W. Huber, *Nat. Rev. Chem.*, 2019, **3**, 223–249.

8 Q. Liu, G. Xu, X. Wang and X. Mu, *Green Chem.*, 2016, **18**, 2811–2818.

9 M. Uyttebroek, W. V. Hecke and K. Vanbroekhoven, *Catal. Today*, 2015, **239**, 7–10.

10 Y. L. Sang, H. P. Jin, S. H. Jang, L. K. Nielsen, J. Kim and K. S. Jung, *Biotechnol. Bioeng.*, 2010, **101**, 209–228.

11 P. Patakova, M. Linhova, M. Rychtera, L. Paulova and K. Melzoch, *Biotechnol. Adv.*, 2012, **31**, 58–67.

12 J. Li, X. Chen, B. Qi, J. Luo, Y. Zhang, Y. Su and Y. Wan, *Bioresour. Technol.*, 2014, **169**, 251–257.

13 X. Wu, G. Fang, Y. Tong, D. Jiang, Z. Liang, W. Leng, L. Liu, P. Tu, H. Wang and N. Jun, *ChemSusChem*, 2017, **11**, 71–85.

14 J. Sun and Y. Wang, *ACS Catal.*, 2014, **4**, 1078–1090.

15 T. Tsuchida, S. Sakuma, T. Takeguchi and W. Ueda, *Ind. Eng. Chem. Res.*, 2006, **45**, 8634–8642.

16 J. Scalbert, F. Thibault-Starzyk, R. Jacquot, D. Morvan and F. Meunier, *J. Catal.*, 2014, **311**, 28–32.

17 Q. Wang, B. Zhou, X. Weng, S. Lv, F. Schuth and A. Lu, *Chem. Commun.*, 2019, **55**, 10420–10423.

18 D. Gabriëls, W. Y. Hernández, B. Sels, P. Van Der Voort and A. Verberckmoes, *Catal. Sci. Technol.*, 2015, **5**, 3876–3902.

19 H. Aitchison, R. L. Wingad and D. F. Wass, *ACS Catal.*, 2016, **6**, 7125–7132.

20 D. Jiang, X. Wu, J. Mao, J. Ni and X. Li, *Chem. Commun.*, 2016, **52**, 13749–13752.

21 J. H. Earley, R. A. Bourne, M. J. Watson and M. Poliakoff, *Green Chem.*, 2015, **17**, 3018–3025.

22 X. Wu, G. Fang, Z. Liang, W. Leng, K. Xu, D. Jiang, J. Ni and X. Li, *Catal. Commun.*, 2017, **100**, 15–18.

23 D. Jiang, G. Fang, Y. Tong, X. Wu, Y. Wang, D. Hong, W. Leng, Z. Liang, P. Tu, L. Liu, K. Xu, J. Ni and X. Li, *ACS Catal.*, 2018, **8**, 11973–11978.

24 T. Tsuchida, J. Kubo, T. Yoshioka, S. Sakuma, T. Takeguchi and W. Ueda, *J. Catal.*, 2008, **259**, 183–189.

25 N. M. Eagan, M. P. Lanci and G. W. Huber, *ACS Catal.*, 2020, **10**, 2978–2989.

26 M. Xue, B. Yang, C. Xia and G. Zhu, *ACS Sustainable Chem. Eng.*, 2022, **10**, 3466–3476.

27 H. Brasil, A. F. B. Bittencourt, K. C. E. S. Yokoo, P. C. D. Mendes, L. G. Verga, K. F. Andriani, R. Landers, J. L. F. Da Silva and G. P. Valença, *J. Catal.*, 2021, **404**, 802–813.

28 J. I. D. Cosimo, V. K. Díez, M. Xu, E. Iglesia and C. R. Apesteguía, *J. Catal.*, 1998, **178**, 499–510.

29 A. J. Scheid, E. Barbosa-Coutinho, M. Schwaab and N. Salau, *Ind. Eng. Chem. Res.*, 2019, **58**, 12981–12995.

30 M. R. Siqueira, O. M. Perrone, G. Metzker, D. C. de Oliveira Lisboa, J. C. Thoméo and M. Boscolo, *Mol. Catal.*, 2019, **476**, 110516–110523.

31 M. León, E. Díaz and S. Ordóez, *Catal. Today*, 2011, **164**, 436–442.

32 D. L. Carvalho, R. Avillez, M. T. Rodrigues, L. Borges and L. G. Appel, *Appl. Catal., A*, 2012, **415**, 96–100.

33 Z. D. Young and R. J. Davis, *Catal. Sci. Technol.*, 2018, **8**, 1722–1729.

34 G. Metzker, J. Vargas, L. Lima, O. M. Perrone and M. Boscolo, *Appl. Catal., A*, 2021, **623**, 118272.

35 Q. Jorge, F. Laura, D. Eva and O. Salvador, *Appl. Catal., A*, 2018, **563**, 64–72.

36 P. Li, Y. Yu, P. P. Huang, H. Liu, C. Y. Cao and W. G. Song, *J. Mater. Chem. A*, 2013, **2**, 339–334.

37 J. Pang, L. He, X. Pan, A. Wang and L. Li, *J. Catal.*, 2016, **344**, 184–193.

38 H. G. Schimmel, J. Huot, L. C. Chapon, F. D. Tichelaar and F. M. Mulder, *J. Am. Chem. Soc.*, 2005, **127**, 14348–14354.

39 J. Mück, J. Kocík and M. Hájek, *Appl. Catal., A*, 2021, **626**, 118380.

40 Z. Xu, J. P. Chada, L. Xu, D. Zhao, D. C. Rosenfeld, J. L. Rogers, I. Hermans, M. Mavrikakis and G. W. Huber, *ACS Catal.*, 2018, **8**, 2488–2497.

41 Q. Wang, X. Weng, B. Zhou, S. Lv, S. Miao, D. Zhang, Y. Han, S. L. Scott, F. Schüth and A. Lu, *ACS Catal.*, 2019, **9**, 7204–7216.

42 X. Fu, X. Ren, J. Shen, Y. Jiang and J. Liang, *Mol. Catal.*, 2020, **499**, 111298.

43 Y. Hong, J. Peng, X. Zhao, Y. Yan, B. Lai and G. Yao, *Chem. Eng. J.*, 2019, **370**, 354–363.

44 K. Sun, F. Song, W. Huang, Y. Tang, Y. Zhang, J. Zhang, Y. Wang and Y. Tan, *Fuel*, 2023, **333**, 126308.

45 A. G. Leon, G. van de Water, B. Leendert and A. Jaap, *J. Catal.*, 2006, **242**, 287–298.

46 B. Hu, W. G. Kim, T. P. Sulmonetti, M. L. Sarazen, S. Tan, J. So, Y. Liu, R. Dixit, S. Nair and C. W. Jones, *ChemCatChem*, 2017, **9**, 3330–3337.

47 Y. Zhao, S. Hyuntae, H. Bo, N. Jens, O. G. Poluektov, J. Tian, D. Massimiliano and A. S. Hock, *ACS Omega*, 2018, **3**, 11117–11127.

48 A. A. Verberckmoes, M. G. Uytterhoeven and R. A. Schoonheydt, *Zeolites*, 1997, **19**, 180–189.

49 E. Kaoutar, K. Mohamed, Z. Mahfoud, A. Souad and B. V. François, *J. Catal.*, 2004, **226**, 16–24.

50 A. Paredes-Nunez, D. Lorito, Y. Schuurman, N. Guilhaume and F. C. Meunier, *J. Catal.*, 2015, **329**, 229–236.

51 A. A. Khassin, T. M. Yurieva, V. V. Kaichev, V. I. Bukhtiyarov and V. N. Parmon, *Mol. Catal.*, 2001, **175**, 189–204.

52 A. Zecchina, G. Spoto, S. Coluccia and E. Guglielminotti, *J. Phys. Chem.*, 1984, **88**, 2575–2581.

53 G. Busca, R. Guidetti and V. Lorenzelli, *J. Chem. Soc., Faraday Trans.*, 1990, **86**, 989–994.

54 Q. Wang, L. Shi, W. Li, W. Li, R. Si, F. Schüth and A. Lu, *Catal. Sci. Technol.*, 2018, **8**, 472–479.

55 J. Pang, M. Yin, P. Wu, X. Li, H. Li, M. Zheng and T. Zhang, *Green Chem.*, 2021, **23**, 7902–7916.

56 Z. Wang, M. Yin, J. Pang, X. Li, Y. Xing, Y. Su, S. Liu, X. Liu, P. Wu, M. Zheng and T. Zhang, *J. Energy Chem.*, 2022, **72**, 306–317.

57 L. Zhang, T. N. Pham, J. Faria, D. Santhanaraj, T. Sooknoi, Q. Tan, Z. Zhao and D. Resasco, *ChemSusChem*, 2016, **9**, 736–748.

58 J. T. Kozlowski and R. J. Davis, *ACS Catal.*, 2013, **3**, 1588–1600.

59 G. Zhang, K. V. Vasudevan, B. L. Scott and S. K. Hanson, *J. Am. Chem. Soc.*, 2013, **135**, 8668–8681.

60 M. R. Li and G. C. Wang, *J. Catal.*, 2018, **365**, 391–404.